Volume 1 | Number 1 | Jan 2013 | Pages 1–100

PCCP

Physical Chemistry Chemical Physics
www.rsc.org/pccp

ROYAL SOCIETY OF CHEMISTRY

ROYAL SOCIETY OF CHEMISTRY

www.rsc.org/pccp

Theoretical study of electronic and tribological properties of *h*-BNC$_2$/graphene, *h*-BNC$_2$/*h*-BN and *h*-BNC$_2$/*h*-BNC$_2$ bilayers

Narjes Ansari,[1] Fariba Nazari,*[1,2] Francesc Illas*[3]

[1]Department of Chemistry, Institute for Advanced Studies in Basic Sciences, Zanjan 45137-66731, Iran

[2]Center of Climate Change and Global Warming, Institute for Advanced Studies in Basic Sciences, Zanjan 45137-66731, Iran

[3]Departament de Química Física & Institut de Química Teòrica i Computacional (IQTCUB), Universitat de Barcelona, C/Martí i Franquès 1, 08028 Barcelona, Spain

Abstract

Density functional theory based methods are used to investigate the interlayer sliding energy landscape (ISEL), binding energy and interlayer spacing between *h*-NBC$_2$/graphene (*I*), *h*-NBC$_2$/*h*-BN (*II*) and *h*-NBC$_2$/*h*-NBC$_2$ (*III*) bilayer structures for three, six and fourteen different stacking patterns, respectively. Our results show that, in the studied cases, increasing the atomic variety of the ingredient monolayers leads to an ISEL corrugation increase as well.

For the studied bilayers the ISEL is obtained by means of the registry index. For sufficiently large flakes of *h*-NBC$_2$ on graphene sheet with the largest incommensurability and the least monolayer anisotropy, a robust superlubricity occurs regardless of the relative interlayer orientation. On the other hand, for the *h*-NBC$_2$/*h*-NBC$_2$ bilayer exhibiting the least incommensurability and the most monolayer anisotropy, the occurrence of robust superlubricity depends on the relative interlayer orientation.

1 Introduction

The development of new tools allowing nanometer-scale measurements and their potential application in nanotechnology constitutes two driving forces in the advances in nanoscale science. The new instruments allow one to probe matter, structures, and surfaces on the nanometer-size scale and provide important information to understand how physics works at these dimensions. In addition, these are often backing the new technologies, namely nanotechnology. Thus, a great deal of activity has focused on building and developing at the atomic-, molecular-, or macromolecular-level devices and structures involving length scales of approximately one to several hundred nanometers. Scanning probes such as Scanning Tunneling Microscope (STM), Atomic Force Microscope (AFM) or SNOM (Scanning Near-Field Optical Microscope) deserve an enormous portion of the credit for the push to both understand and exploit nanometer-scale phenomena.[1]

One area that has greatly benefited from the efforts mentioned above is tribology. The term derives from the Greek root "tribo" that means to rub, grind, or wear away; in general. Hence, tribology is defined as the science and technology of interacting surfaces in relative motion, which involves friction, wear, and lubrication.[2,3] In particular, tribology of automotive applications has been studied for decades but the application to microelectromechanical systems (MEMS), magnetic storage devices, adhesive contacts, micro/nanotribology and biotribology constitutes a new field. Nanotribology, tribology at the nanoscale, constitutes a relatively new field that uses nanotechnological methods to deal with friction, wear, and lubrication of interacting surfaces in relative motion,[4-11] with the ultimate goal of boosting the performance of nanosystems.[12]

The development of green nanotribology requires handling nanosurfaces, nanoagents (ingredients, additives), and nanoprocesses. Here, nanosurfaces stand for two-dimensional objects used in tribology that aim at adding additional functionality to the tribosystems via the physical properties of the interfaces (as opposed to bulk chemistry). Graphene and graphene-like structures are the nanosurfaces that could become important for microelectronics.[13] For instance, researchers applied one such 2D layered material, to produce improved transistor performance at an industrially relevant scale.[14] Nanosurfaces are also being considered as hypersensitive sensors, in catalysis, tissue engineering and energy storage as well.

Regarding graphene-like surfaces, it is well known that hexagonal boron nitride (*h*-BN) closely resembles elemental carbon structures by sharing the same total number of electrons between the neighboring atoms.[15-17] Both, graphene and *h*-BN structures have become an important subject of research, owing to their mechanical strength and a rich variety of physical phenomena connected to their electronic structure.[18] The structural similarities between graphene and *h*-BN allow them to form essentially seamless in-plane hybrids with continuously tunable C:BN stoichiometry.[16] A hybrid atomic monolayer, hereafter referred to as *h*-BNC, of hybridized phases of *h*-BN and graphene would have interesting properties by combining those of two seemingly disparate materials with similar lattice parameters and crystal structure.[16] Thus, *h*-BNC is an interesting material that would enable the tailoring of physical properties in graphene-based structures by varying the ratio of C and BN in these materials. Interestingly, *h*-BN–graphene heterolayer structures were first prepared about 20 years ago.[19]

Composite systems must be structurally stable and should not unduly modify the individual character of each material.[20] They can be roughly divided into in-plane and interlayer (or heterolayer) categories. Precisely, this possibility has renewed interest in 2D hexagonal BNC sheets[21-24] even if work on *h*-BCN structures has been going on for decades[25-27]. All theoretical studies at various levels of theory[22,23,28] as well as experiments,[29] indicate that for the C and BN regions it is energetically favorable to completely phase separate in *h*-BNC sheets. Composites of graphene and BN containing boron, carbon and nitrogen in varying proportions are usually referred to as $B_xC_yN_z$,[30] these composite can possess hexagonal BCN networks and photoluminescence measurements indicate that the gap appears to be smaller in carbon-rich samples.[31]

Examining these composite structures at the nanoscale provides insight into tribological processes. This is simply because at the scale of a few tenths of nanometers to a few nanometers surfaces are not atomically flat. Surface roughness is made of microscopic bumps strongly interacting with each other. Precisely, lubricants add a layer of fluid between the bumps to decrease the interaction between these microscopic irregularities often leading to deterioration of the material as their surfaces slide into each other. Because of the surface roughness, the forces and stresses between the interacting surfaces can be much higher than what one would calculate from a gross applied force per total area. In the case of sliding contacts, the high stresses generated by contacting asperities dominate and can lead to extreme temperatures, deformation,

and for some materials even welding and subsequent tearing of asperities.[13, 32] With the new tools of nanotechnology, the exploration of mechanical properties at the nanoscale became possible and new phenomena discovered. One important discovery from these nanometer scale friction studies is the frequent breakdown of the phenomenological friction laws[6,10] implying that there is interesting physics yet to be revealed. The extent of friction is proportional to the contact area and interfacial shear strength produced by the surface load. However, while surface load is a well-defined and measurable quantity, the contact area is a quantity that is harder to define and subject to interpretation. This has given rise to a controversy over which is the fundamental controlling parameter: load as in the original law or contact area. This controversy is still active today. The reason why the contact area is not a well-defined quantity is due to the enormous range of the strength of the various forces between atoms involving van der Waals, electrostatic, and chemical bonding interactions. These forces also vary dramatically in their distance dependence. The strong forces responsible for chemical bonding and for repulsion arise from the overlap of atomic orbitals and decay exponentially within angstrom distances. The interlayer potential landscape in layered materials is essential for understanding their mechanical and electromechanical behavior.[13] For example, nanoelectromechanical systems (NEMS) based on low dimensional structures often rely on mechanical deformations such as twisting[13, 32, 33] and bending.[34-36] In addition, the anisotropy of the ingredient monolayers affects structural and electromechanical properties of the bilayers.

Inspired by the recent work of Hod et al. on the possibility of the robust superlubricity— the state of vanishing friction— in graphene/h−BN heterojunctions,[37] the present work explores the interlayer sliding energy landscape (ISEL) and registry index (RI) corrugation of three bilayer model systems from first principles.

2 Models and computational details

The main goal of the present work is to determine electromechanical properties of bilayers of 2D materials. In particular, we focus on ISEL, registry index and RI corrugation. To this end, the selection of monolayers as the building block of bilayers constitutes an important issue. We already mentioned that the structural similarities between graphene and the h-BN sheet allow them to form essentially seamless in-plane hybrids with continuously tunable h-$(BN)_xC_y$ stoichiometry.[16] Song et al.[38] synthesized h-$(BN)_xC_y$ sheets through chemical vapor deposition (CVD) and found that these have domains of graphene and h-BN within the hexagonal sheets.

Hence, we select the h-$(BN)_xC_y$ unit cell with the lowest energy structure as introduced by Zhu et al.[39] and consider x=1 and y=2; the corresponding unit cell consists of four C, two nitrogen and two boron atoms (Fig. 1a).

Three different bilayers are built, two heterogeneous systems combining one h-BNC_2 monolayer with graphene and h-BN and one homogeneous system having two h- layers. The unit cell of h-NBC_2/graphene, h-NBC_2/h-BN and h-NBC_2/h-BNC_2 bilayers consists of 16 C and/or N and/or B atoms in the periodic sheets. For strained two-layer models the lattice vectors of both layers are constrained to be identical, the lattice constant and coordinates of all unit-cells are depicted in Table S1 in the Supporting Information. Nevertheless, for unstrained bilayers, both the cell dimensions along the sheets growth directions and the atomic positions are allowed to fully relax until the forces acting on each atom are smaller than 0.001 eV/Å (Table S2). In order to simulate the candidate layer and/or bilayer systems, a density-functional theory (DFT) method with dispersion (DFT-D) correction[40] has been used as in the PWSCF code of the Quantum ESPRESSO suite[41]. The DFT calculations use the (PBE) form[42] of generalized gradient approximation (GGA) exchange-correlation density functional. It is well documented[43,44] that GGA exchange-correlation density functional tends to largely underestimate the band gaps.

The density is expanded in a plane wave (PW) basis set and the effect of atomic cores is included through ultrasoft pseudopotentials (US-PP).[45,46] For the 16 atoms unit cell containing h-NBC_2 on a graphene or h-BN or h-NBC_2 layer a kinetic energy cutoff of 460 eV was selected and integration in the reciprocal space used a mesh of $6 \times 12 \times 1$ k points. The energy convergence for all electronic steps was set at 10^{-8} a.u. Periodic 2D boundary conditions are considered along the growth directions of the sheets, and a sufficiently large vacuum spacing of 20 Å in perpendicular direction of surface was used to prevent unwanted interactions between adjacent layers. Figure 1b-d shows schematically the relaxed unit cell of strained heterogeneous h-NBC_2/graphene, h-NBC_2/h-BN and homogeneous h-NBC_2/h-NBC_2 bilayers. For simplicity, the h-NBC_2/graphene, h-NBC_2/h-BN and h-NBC_2/h-NBC_2 bilayers are denoted *I*, *II* and *III*, respectively. Interlayer binding energies between the *I*, *II* and *III* bilayers for three, six and fourteen different stacking patterns are calculated as:

$$\Delta E = \frac{1}{2}(E_{12} - (E_1 + E_2)) \qquad (1)$$

where E_{12} is the total energy of the system containing the two interacting layers, E_1 and E_2 is the total energy of each isolated graphene or h-BN or h-NBC$_2$ mono-layer. The relative interlayer interaction is calculated as follows:

$$e_{eq} = \Delta E - E_{AB} \tag{2}$$

where ΔE is the binding energy of the different stacking patterns and E_{AB} is the binding energy of the optimal stacking mode. The maximum differences of the equilibrium energies and distances are defined as

$$\Delta e_{eq} = e_{max} - e_{min} \tag{3}$$

and

$$\Delta Z_{eq} = Z_{max} - Z_{min} \tag{4}$$

respectively, where e_{max} and e_{min}, are the binding energy of the worst and optimal stacking modes and Z_{max} and Z_{min} are the equilibrium distance of the worst and optimal stacking modes in each model system.

Following the work of Marom et al.[47], the main features of the ISEL can be captured by means of a simple registry index (RI), a numerical parameter providing a proficient and unswerving tool for quantifying the registry mismatch in bilayer systems and mimicking their corrugated sliding energy landscape. In this approach, a circle with a given radius r_i; which in principle can be obtained from appropriate fitting (see next section) is assigned to each atom i in the unit cell and centered on it. Next, the overlap between the projection of circles (S_{ij}) assigned to atoms located on one layer with circles associated with atoms belonging to the other layer are calculated. The overlap elements are appropriately summed to produce a simple numerical measure of the overall registry mismatch ($RI \propto \sum \pm S_{ij}$). This numerical value is then normalized to the range [0-1], where 0 represents perfect interlayer registry and 1 stands for the worst stacking mode in terms of the total energy. RI is a dimensionless parameter. As we aim at comparing the ISEL of DFT-D with the one calculated by RI method, the scaling factor (SF) is used. SF is defined as the difference between binding energy of the optimal and worth stacking mode for each of I, II and III model systems. To do this we have defined the optimal stacking mode with the lowest energy as 0 meV/unit cell. By multiplying the scaling factor, per unit of energy, to RI we can obtain the ISEL of RI in the range of DFT-D based ISEL.

To optimize the fit between RI predictions and first-principles calculations we used a simple Genetic Algorithm in the MATLAB programming language. To assess the accuracy our

written MATLAB code to calculate the RI, the corrugation of bilayers graphene/graphene [48,49] and h-BN/h-BN[47-49] have been obtained. The radii of the circles employed in this work are r_C=0.5 L_{CC}, r_N= 0.5 L_{BN} and r_B =0.15 L_{BN}, where L_{CC}=1.421Å, L_{BN}=1.45Å. The reported values for RI of the graphene/graphene[48,49] and h-BN/h-BN[47-49] bilayers are in good agreement with those obtained in the present work (Fig. S1).

3 Results and discussion

3.1 Energetics of the geometrical structures

The physical properties of the stacked monolayers leading to the bilayer structures, of interest depend on interlayer interactions[48], the different nature of the intra- and inter-layer interactions leading to highly anisotropic properties of the resulting layered systems. The registry matching between the interacting layers is an important descriptor of the physical properties of bi-layered systems. Hence, the identification of high-symmetry stacking modes becomes crucial. In this study, all possible high-symmetry stacking orders for strained h-NBC$_2$/graphene, h-NBC$_2$/h-BN and h-NBC$_2$/h-NBC$_2$ bi-layer systems are considered which are depicted in the inset of Fig. 2-4. In the *I*, *II* and *III* model systems the atomic type variety of the bottom layer increases, consequently the number of high-symmetry stacking orders leads to 3, 6, and 14 different eclipsed and/or staggered stacking modes, respectively.

In the unit-cell of strained h-NBC$_2$/graphene, three important high-symmetry stacking modes can be identified namely staggered with C and B over C (AB$_I$); staggered with C and N over C (AB$_{I-1}$) and eclipsed with C, N and B over C (AA$_I$); see inset in Fig. 2. In a similar way, six possible high-symmetry stacking modes are recognized in the unit-cell of h-NBC$_2$/h-BN bilayer (see inset of Fig. 3). These are the staggered with C and N over B (AB$_{II}$); the staggered with C and B over B (AB$_{II-1}$); the staggered with C and B over N (AB$_{II-2}$), the eclipsed with C over N or B and N over B (AA$_{II-1}$), the staggered with C and N over N (AB$_{II-3}$) and, finally, eclipsed with C over N or B and N(B) over N(B) (AA$_{II}$). In the case of the h-NBC$_2$/h-NBC$_2$ system, because of the increasing atomic type variety in the bottom layer, six different possibilities exist for the interactions between atoms. This is C(N, B) with C(N, B), C(N) with N(C), C(B) with B(C) and N(B) with B(N). For simplicity, the interactions are denoted as CC, NN, BB, CN, CB and NB, respectively. Following the same logic for the third model system (h-NBC$_2$/h-NBC$_2$), fourteen suggested high-symmetry stacking modes can be identified, which are

represented in the inset of Fig. 4. These can be described as: the staggered with two CN and two CB overlapping (AB_{III}); the staggered with two CC and two BB fully overlapping (AB_{III-1}); the staggered with one CC, one BB and two CB fully overlapping (AB_{III-2}); the staggered with four CB full overlap (AB_{III-3}); the staggered with one CC, CN, CB and one NB full overlap (AB_{III-4}); the eclipsed with two CC, CN, CB and NB full overlap (AA_{III-1}); the staggered with two CC and CB full overlap (AB_{III-5}); the eclipsed with four CC and NB full overlap (AA_{III-2}); the staggered with one CC and NN and two CN full overlap (AB_{III-6}); the eclipsed with four CN and CB overlapping (AA_{III-3}), the staggered with four CN fully overlapping (AB_{III-7}); the staggered with two CC and NN overlap (AB_{III-7}); the eclipsed with two CC, CN and CB and one NN and BB full overlap (AA_{III-4}) and, finally, the eclipsed with four CC and two NN and BB full overlap (AA_{III}).

In each of the three model systems, one can readily see that it is possible to transform one stacking mode into another by horizontal layer sliding and/or by rotation around the vertical axis and, hence, the transformation is closely related to friction at the atomic level. To obtain the order of stability and equilibrium distance (Z_{eq}) for each model systems in each of the different high-symmetry stacking modes we rely in the binding energy calculated as in Eq. 1 and varying interlayer distance from ~2 Å to 9 Å while fixing the in-plane lattices. These calculations start from the DFT based method structure data given in Table S1. The obtained data for the studied bilayers at all high symmetry stacking modes are reported in Fig. 2-4, respectively. The interaction energy curves for the different stacking configurations of the all three bilayers in Fig. 2-4 shows that the largest and smallest interaction energies correspond to the eclipsed and staggered orientations, which are not unexpected since these, are known to provide the optimal and worst stacking modes, respectively. For the *I*, *II* and *III* bilayers, the worst stacking modes are the AA_I, AA_{II} and AA_{III} configurations, in which the lattices of the two layers are fully eclipsed, whilst the optimal stacking modes are the AB_I, AB_{II} and AB_{III} configurations, respectively. The inset of Fig. 2-4 clearly displays this information. In principle, the lower stability of the AA stacking mode in all studied cases could be attributed to a more repulsive force between the two layers due to the stronger Pauli repulsions. However, this is not always the case. In fact, in the intermediate configurations there are not clear trend between the interaction energies of eclipsed and staggered models. Fig. 5 shows the numerical values obtained for relative interlayer interaction energy (e_{eq}) of all high symmetry stacking modes of three studied

systems. From the binding energy curves in Fig. 4 it is evident that the eclipsed AA_{III-1}, AA_{III-2} and AA_{III-3} configurations exhibit a trend similar to those of the staggered AB_{III-5}, AB_{III-6} and AB_{III-7} stacking modes, respectively. The AA_{III-1}, AA_{III-2} and AA_{III-3} configurations are more stable than the AB_{III-5}, AB_{III-6} and AB_{III-7} pattern by approximately 0.44, 0.25 and 0.44 meV per atom, respectively. In some cases even stacking modes with eclipsed structures are more stable than staggered models (in the h-NBC$_2$/h-BN bilayer, the AA_{II-1} is ~ 4.5 (meV/atom) more stable than the AB_{II-3} configuration). This can be rationalized by the fact that there is enhanced Pauli repulsion between eclipsed N atoms in the AB_{II-3} mode and by the monopolar electrostatic interaction between the partially charged N and B sites in the AA_{II-1} mode.

It is worth to emphasize that for the h-NBC$_2$/h-NBC$_2$ model system the AB_{III} stacking mode is just 0.14 meV/atom less stable than the AB_{III-1} configuration. These two structures can be transformed into each other by the basal plane rotation around the c axis and the subsequent sliding mode. This small energy difference suggests that in the h-NBC$_2$/h-NBC$_2$ model system, these two stacking modes are equally optimal. The inset of Fig. 5 reports the Δe_{eq} and ΔZ_{eq} trends and shows that changing the bottom layer from G to h-BN or h-BNC$_2$, the Δe_{eq} increases steadily and in equal footing with ΔZ_{eq} .

The electrostatic forces, mainly Pauli repulsion, dictate the optimal stacking mode and the interlayer sliding energy.[50] Therefore, these trends are indicating the strong Pauli repulsion interaction between h-BNC$_2$/h-BNC$_2$ layers in comparison with h-BNC$_2$/h-BN and h-BNC$_2$/graphene bilayers. As mentioned above, in the I, II and III model systems both intra and inter-layer interactions play an important role in determining the final electronic properties of these systems. In order to shed light on the intra-layer interactions, the band structure of the graphene, h-BN, and h-BNC$_2$ monolayer systems are presented in Fig. 6a-6c. The results show that graphene is a semimetal with band gap zero closing at K point in the reciprocal space. However, due to the ionic characteristics of the B–N bonds, h-BN is a wide band gap (4.96 eV) electric insulator and a pure h-BNC$_2$ sheet is a semiconductor with a band gap of 1.19 eV. All band gaps calculations are performed using the GGA functional.The different intra-layer interactions are clearly responsible for the electronic differences and, in turn, the former originate from the different atomic types in these 2D isoelectronic hexagonal monolayers. It is worth to emphasize that there is a positive relation between the charge transport character and concentration of carbon atom per unit cell. The charge transport character increases ($E_{g-G} \approx 0 > E_{g-}$

$_{h\text{-}BNC_2}\approx 1.19 > E_{g\text{-}h\text{-}BN}\approx 4.96$ eV) as the number of carbon atoms per unit cell increases ($C_{num\text{-}G}=8 > C_{num\text{-}h\text{-}BNC_2}=4 > C_{num\text{-}h\text{-}BN}=0$) in graphene, $h\text{-}BNC_2$ and $h\text{-}BN$ monolayer, respectively.

The variety in atomic composition in the bottom layers in the bilayer systems along with interlayer interactions, which hold the sheets together, cause the whole system to exhibit clear different electronic behavior in comparison to the isolated individual monolayers. Based on the above considerations, we analyze the band structure of selected stacking modes of the *I*, *II* and *III* model systems. In order to study the effects of inter-layer interactions in the electronic properties, we select the worst and optimal stacking modes of *I*, *II* and *III* model systems as a sample modes. The DFT based calculations show band gap opening in the all these structures. Similar to the previous cases for the monolayer systems, a linear relation between the charge transport character and concentration of carbon atom per unit cell in three bi-layer systems can be clearly seen. For each model system, we now consider the stacking mode with maximum band gap opening.

In the AB stacking mode of the model system *II* with 4-carbon atom per unit cell, the band gap reaches a maximum of 1.25 eV (Fig. 6f). The band gap of AB stacking mode of the model system *III* with 8 carbon atom per unit cell decreases to 0.659 eV (Fig. 6e). The lowest band gap opening (0.163eV, Fig. 6d) is related to the AA stacking mode of the model system *I* with the maximum number of carbon atoms per unit cell (12/16 carbon atom). Finally, the non-polar nature of the homo-nuclear C-C interactions between layers may result in an increase in the charge transport character in these systems.

3.2 Obtaining the Registry Index

In order to quantify the RI the radii of the circles assigned to each atomic species need to be known. In the present work, this single parameter is obtained from fitting the interlayer sliding energy landscape predicted from RI to that obtained from the DFT calculations. To this end, a series of DFT calculations have first been launched to define this ISEL. Sliding was modeled by dragging the upper layer with respect to the underlying hexagonal bottom layer in 75×20 grid of lateral shifts in a rectangle region. The sliding was started from an eclipsed orientation and stopped in the next eclipsed orientation. Fig. 7a-7c display the ISEL for three *I*, *II* and *III* model systems at constant $Z_{eq\text{-}min}$. Next, by using the simple genetic algorithm in the MATLAB programming language, a good fit between the RI predictions and ISEL first-

principles calculations is obtained. The radii of atoms are chosen among those predicted by the GA.

The fact that different radii of the C, N, and B atoms are obtained for each of the studied systems reflects the non-uniform charge distributions around atoms in each system. Obtained radii are then used to assess the RI $\propto \sum \pm S_{ij}$ values following the procedure outline in Ref[49]. The RI results for the *I, II* and *III* candidate model systems described below provide a comprehensive picture of the relative stability of the different stacking modes.

For system *I* (h-BNC$_2$/graphene), the worst and/or optimal stacking modes (AA$_I$ and AB$_I$) are examined and three different types of overlaps are considered (see Fig. 1e). These are S_{CC}, S_{CN} and S_{CB} which are the projected overlap between circles assigned to a carbon atom in the graphene layer and circles associated with the carbon, nitrogen, or boron atoms of the h-BNC$_2$ layer, respectively. Note also that each S_{ij} element is representative of the projected overlap between circles assigned to the atoms of top and bottom layers. At the optimal stacking mode, S_{CN} is minimal and that at the worst stacking mode all overlaps exhibit a maximal value. Following previous works[37,49], we define the RI to be proportional to the sum of all overlaps, RI $\propto S_{CC} + S_{CB} + S_{CN}$. With this definition, RI exhibits a minimum value at the optimal stacking mode and a maximum at the worst staking mode, similar to the total energy of the bilayer system. Next, we normalize the RI to the range [0:1] as in Eq. (5)

$$R_{h-BNC_2/graphen} = \frac{(S_{CC}-S_{CC}^{AB})+(S_{CN}-S_{CN}^{AB})+(S_{CB}-S_{CB}^{AB})}{(S_{CC}^{AA}-S_{CC}^{AB})+(S_{CN}^{AA}-S_{CN}^{AB})+(S_{CB}^{AA}-S_{CB}^{AB})} \tag{5}$$

In Fig. 7a and 7d, we compare the sliding RI surface calculated for different interlayer positions of the h-NBC$_2$/graphene heterojunction and the sliding energy landscape calculated using the PBE functional. As mentioned above to obtain good correspondence between the two surfaces, we choose $r_C = 0.7155$ Å, $r_N = 0.69$ Å, and $r_B = 0.1$ Å, where for the case of the strained unit-cell, all CC, CN, CB and NB bond lengths are taken to be equal, $L_{CC}= L_{CN}=L_{CB}=L_{BN} = 1.431$ Å. The agreement between the sliding energy landscape calculated from the relaxed structure and the sliding RI surface presented in Fig. 7a and 7d suggests that a simple scaling factor of 98.22 meV/unit cell in the present case may be used to relate the results of the RI calculations to sliding energies obtained via advanced DFT methods for such systems.

Let us now consider the results for model system *II* (*h*-BNC$_2$/*h*-BN). Here, five different types of overlap elements need to be considered for the worst and/or optimal stacking modes. These are S_{CN}, S_{CB}, S_{NN}, S_{BB} and S_{NB} (Fig. 1e). In this case, for the optimal stacking mode only S_{CB} and S_{NB} are present and for the worst stacking mode all overlaps are of maximal value. Consequently, the RI is now obtained as in Eq. (6)

$$R_{h-BNC_2/h-BN} = \frac{(S_{CN}-S_{CN}^{AB})+(S_{CB}-S_{CB}^{AB})+(S_{NN}-S_{NN}^{AB})+(S_{BB}-S_{BB}^{AB})-(S_{NB}-S_{NB}^{AB})}{(S_{CN}^{AA}-S_{CN}^{AB})+(S_{CB}^{AA}-S_{CB}^{AB})+(S_{NN}^{AA}-S_{NN}^{AB})+(S_{BB}^{AA}-S_{BB}^{AB})-(S_{NB}^{AA}-S_{NB}^{AB})} \qquad (6)$$

where values of 0 and 1 correspond to optimal and worst stacking modes, respectively. Fig. 7e shows the calculated RI surface for different interlayer positions of the heterojunction structure *II* with r_C=0.7155Å, r_N=0.6276Å, r_B=0.2868Å. Similar to the previous model system, a scaling factor of 115.58 meV/unit cell may be used to relate the results of the RI calculations to sliding energies obtained via the PBE exchange-correlation functional approximation of DFT. It should be mentioned that for the strained unit cell CC, CN, CB, and NB bond lengths are taken to be equal, L_{CC}= L_{CN}=L_{CB}=L_{BN} = 1.431 Å.

Defining properly the RI of the model system *III* (*h*-BNC$_2$/*h*-BNC$_2$) and because of the atomic complexity it is necessary to consider six different types of overlap, again for the optimal and worst stacking modes (Fig. 1e). These are S_{CC}, S_{NN}, S_{BB}, S_{CN}, S_{CB} and S_{NB} where the notation is as in systems *I* and *II*. Normalization of the RI for system *III* is as in Eq. (7)

$$R_{h-BNC_2/h-BNC_2} = \frac{(S_{CN}-S_{CN}^{AB})+(S_{CB}-S_{CB}^{AB})+(S_{CC}-S_{CC}^{AA})+(S_{NN}-S_{NN}^{AA})+(S_{BB}-S_{BB}^{AA})-(S_{NB}-S_{NB}^{AA})}{(S_{CN}^{AA}-S_{CN}^{AB})+(S_{CB}^{AA}-S_{CB}^{AB})+(S_{CC}^{AA}-S_{CC}^{AB})+(S_{NN}^{AA}-S_{NN}^{AB})+(S_{BB}^{AA}-S_{BB}^{AB})-(S_{NB}^{AA}-S_{NB}^{AB})} \qquad (7)$$

By setting r_C=0.7155Å, r_N=0.5500Å, r_B=0.1500Å, we obtained good agreement between RI and calculated ILSE from DFT. In this case, a simple scaling factor that relates ISEL to RI is 172 meV/unit cell.

3.3 Analysis of RI corrugation

In order to investigate the superlubricity of the *I*, *II* and *III* model systems we analyze the topology of the RI. In this respect, we follow the procedure described by Hod et al.[37] quite recently.

First, a finite square rigid h-BNC$_2$ flake of a given size is chosen (Fig. S2a) and arranged in such a way that the center of mass of the flake corresponds to the origin of the coordinate system (Fig. S2b). Next, to build the appropriate rigid *I*, *II* and *III* bilayer model systems, a monolayer of G, h-BN or h-BNC$_2$ is placed below the flake again in such a way that the center of mass of the monolayer is exactly below the center of mass of the corresponding flake (Fig. S2c). The overall resulting systems are described in Fig. 8a, 9a and 10a, respectively. According to ref 37, the rigidity assumption can be justified in materials in which their intralayer/bulk Young modulus is considerably higher than the interfacial shear modulus. The Young modulii of graphene ($\sim$1.0 TPa) [51,52] and h-BN (0.811 TPa)[53] are considerably higher than the corresponding interlayer shear modulii of graphite (4.3−5.1 GPa)[53-55] and h-BN (7.7 GPa)[53]. On the other hand, h-BNC$_2$ being a combination of these materials, is expected to exhibit the properties of the two extremes. Peng et al.[56] show that the Young moduli of h-BNC$_2$ is in the middle of graphene and h-BN.

In order to obtain information about friction between the constituting layers, the upper h-BNC$_2$ flake is now either rotated or displaced.[57] Rotation involves an axis crossing the center of mass by the required misfit angle which goes from -20° to +80° as illustrated in Fig. 8b to 10b for systems *I*, *II* and *III*, respectively. Displacements involve lateral shifts of the rotated h-BNC$_2$ flake parallel to the armchair axis of the G, h-BN and h-BNC$_2$ supercells. For each angle, the RI amplitude is calculated for various displacements as indicated in the previous section and results plotted. The overall procedure is repeated for flakes of different sizes. Fig. 8b, 9b and 10b show the maximum values of corrugation for the registry index (RI$_{max}$) as a function of misfit angel for several rectangular h-BNC$_2$ flakes of various sizes on the graphene, h-BN and h-BNC$_2$ layers. Here, RI$_{max}$ is representative of maximal variations of the RI calculated along linear paths in the sliding direction as a function of interlayer misfit angle.

Let us now consider in some detail the topology of the RI$_{max}$ for each one of the studied systems. For the smallest flake size (2 × 2 with x=5, y=10) of h-BNC$_2$ on graphene, the sixfold symmetry of the bottom layer implies a large corrugation for misfit angles of 0° and 60°. It is because, in this case due to the homogeneity of the graphene monolayer, both degrees are associated with the AA stacking mode. For intermediate misfit angles, a qualitatively different behavior emerges. By increasing the flake size, the overall RI corrugation reduces steadily up to the point where for the 72 × 42 h-BNC$_2$ flake with x=3045, y=6090 , the maximum RI

corrugation recorded is less than 10% of that calculated for a strained flake (with no h-BNC$_2$/graphene lattice mismatch) of the hexagonal lattice. Using the scaling relation obtained above (6.14 meV/atom), the maximal sliding energy corrugation for this flake is estimated to be ~0.55 meV/atom. This value is comparable to that reported by Hod (~0.62 meV/atom) for graphene/h-BN system[37] and thus resulting in a superlubricity exhibiting stable state for h-BNC$_2$/graphene.

Like in the graphene/h-BN junction [37], in model system *I*, the existence of lattice mismatch between the top and bottom layer results the formation of clear Moiré patterns. The presence of top monolayer heterogeneity, h-BNC$_2$, in the model system *I*, is the clear difference between our h-BNC$_2$/graphene model system and the graphene/h-BN junction[37]. These cases imply that, for sufficiently large flakes with concomitant reduced lattice commensurability, frictional anisotropy will be considerably reduced.

In the model system *II*, the presence of N and B atoms in the lattice of the bottom layer and of C, N and B atoms in the top layer results in asymmetric high friction peaks at 0° and 60° even for the smallest flake size (2×2). This behavior clearly originated by the different atomic type interactions. For instance, for the 0° misfit angle, the system is in the worst staking mode with maximum repulsion between overlapping NN and BB atoms. However, by rotating the top layer by 60°, the repulsive NN and BB overlapping changes to the favorite NB overlap (see Fig. 9b). As a result, at the 60° misfit angle, according to Eq. (6), increasing the amount of NB overlap in comparison to NN and BB overlaps, reduces the RI corrugation .

By increasing the flake size, the difference between the height of peaks at 0° and 60° becomes even larger. For the 72×42 h-BNC$_2$ flake above the h-BN bottom layer, the maximum RI corrugation is over 40% of that calculated for a strained flake (with no h-BNC$_2$/ h-BN lattice mismatch) of the hexagonal lattice. Using the scaling relation reported in the previous section (7.22 meV/atom), the maximal sliding energy corrugation for this flake is estimated to be ~3.18 meV/atom. It is clear that in such system because of tiny mismatch and large amount of Pauli repulsion a larger flake is needed to attaine an overall vanishingly small friction.

We finally comment on the model system *III* where the stacking of h-BNC$_2$ flake on the h-BNC$_2$ monolayer results in a homogenous junction. In this system, the existence of three types of atoms in the lattice of the flake and bottom layer produce anisotropy in the RI corrugation. As a result, for the smallest flake size (2×2) the high friction peaks at 0° and 60° remain asymmetric.

This is similar to the previous case, h-BNC$_2$@h-BN. However, at 0°, due to the lack of mismatch between h-BNC$_2$ flake and h-BNC$_2$ bottom layer and the maximum amount of CC, BB and NN overlaps, see Eq. (7), the maximum RI corrugation attains its highest value. However, by rotating the top layer by 60°, the later repulsive CC, NN and BB overlapping changes to the favorite NB and CB overlaps (see Fig. 9b). As a result, in the 60° misfit angle, according the Eq. (7), increasing the amount of NB and CB overlaps in comparison to CC, NN and BB overlaps, reduces the RI corrugation. In this case, using the scaling factor reported in the previous section, the maximal sliding energy corrugation for all different size of flake will be ~10.75 meV/atom.

However, because of the heterogeneity within the flake and also within the bottom layer, upon increasing the flake size leads the maximum of RI corrugation at 60° to less than 10% of that calculated for a strained flake. Using the scaling relation obtained above (~10.75 meV/atom), the maximal sliding energy corrugation for this flake at the 60° is estimated to be ~0.9 meV/atom (see Fig. 10b). Therefore, in this model system even if the bilayer is homogenous, the intrinsic heterogeneity of the layers a robust superlubricity is predicted to occur at a mismatch angle of 60°. This is in contrast to the case of the homogeneous graphene interface where flake reorientations are known to eliminate superlubricity[37]. It is worth to emphasize that the RI corrugation in the systems with hexagonal symmetry strongly is related to two factors: 1) the homogeneity or heterogeneity of flake and/or monolayer and 2) the homogeneity or heterogeneity of bilayers. The existence of each of the factors will induce superlubricity even in the 0° and/or 60° angles. The clear difference is related to occurrence of robust superlubricity. The latter case only can be observed in the heterogeneous bilayers with hexagonal symmetry.

4 Conclusions

In the present work, the interlayer sliding energy landscape (ISEL), binding energy and interlayer spacing of two heterogeneous h-NBC$_2$/graphene (*I*), h-NBC$_2$/h-BN (*II*) and one homogeneous h-NBC$_2$/h-NBC$_2$ (*III*) bilayers have been determined from density functional theory based calculations including dispersion contributions. In each case, different high symmetry stacking patterns have been considered. In the *I*, *II* and *III* model systems the atomic type variety of the bottom layer increases with a concomitant increase in the number of high-symmetry stacking leading to 3, 6, and 14 different eclipsed and/or staggered stacking modes, respectively. In all studied cases, the worst stacking modes are the AA$_I$, AA$_{II}$ and AA$_{III}$

configurations, in which the lattices of the two layers are fully eclipsed, whilst the optimal stacking modes are the staggered AB_I, AB_{II} and AB_{III} configurations, respectively. The interlayer sliding-energy landscape of the *I*, *II* and *III* model systems show that by decreasing the incommensurability between lattices of bilayers (*III* < *II* < *I*) the ISEL corrugation and, accordingly, the Pauli interaction between layers increases, respectively.

The variety of the bottom layers in the bilayer systems along with interlayer interactions, which holds the sheets together, cause to whole system to exhibit clear different electronic behavior, especially in comparison with individual monolayers. In particular, the present first-principles electronic structure calculations predict a clear band gap opening all structures studied. The minimum and maximum band gap opening related to the AA_I and AB_{II} stacking modes with the largest and smallest number of carbon atoms per unit cell. The non-polar nature of the homo-nuclear C-C interactions between layers may result in an increase in the charge transport character in these systems.

A simple registry index (RI) method has been derived which is able to accurately capture the DFT based interlayer sliding-energy landscape of the three h-NBC_2/graphene, h-NBC_2/h-BN and h-NBC_2/ h-NBC_2 bilayer systems. The RI thus defined is then used to explore the sliding physics of heterogeneous h-NBC_2/graphene , h-NBC_2/h-BN and homogeneous h-NBC_2/ h-NBC_2 interfaces. The results indicate that for an h-NBC_2 flake sliding on top of graphene, h-BN, and h-NBC_2 layers anisotropy of the monolayers and degree of commensurability between the lattices of the flake and the underlying layers play a major role in the occurrence of superlubricity.

For sufficiently large flakes of h-NBC_2 on a graphene sheet with the most incommensurability and the least monolayer anisotropy a robust superlubricity is predicted regardless of the relative interlayer orientation. For the heterogeneous h-NBC_2/h-NB junction with moderate incommensurability and anisotropy long periodic h-NBC_2/h-NB Moiré superstructures are required to decrease the friction to achieve a robust superlubricity. Finally, for the homogeneous h-NBC_2/h-NBC_2 junction with the smallest degree of incommensurability, and the largest monolayer anisotropy, the occurrence of robust superlubricity largely depends on the relative interlayer orientation.

Acknowledgements

Figure 1.- (a) Unit cell of h-BNC$_2$. (b), (c) and (d) Schematic representation of the optimized strained *I, II* and *III* model systems, respectively. The interlayer distance was kept fixed at 3.15 Å. (e) All various possibility for registry-index definition of the projected overlap area between circles of the upper h-BNC$_2$ atoms (transparent circles, which are B or N or C) with the lower graphene, h-BN or h-BNC$_2$ atoms (opaque circles, which are B or N or C) in the *I, II* or *III* model systems.
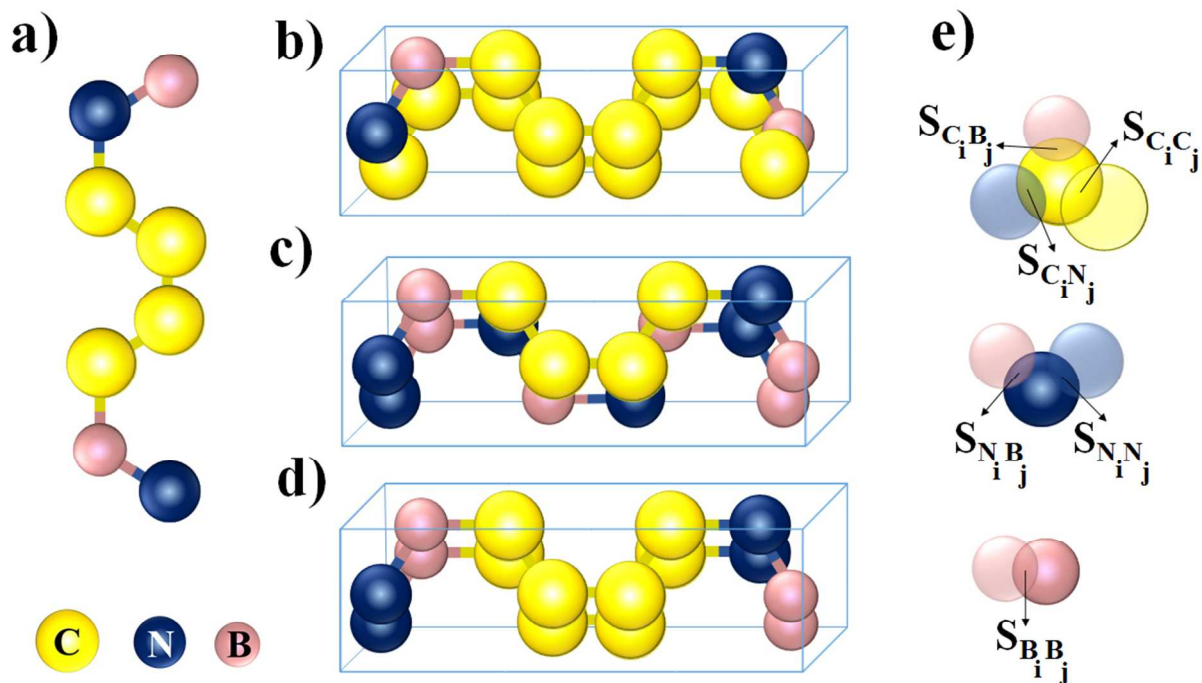
Figure 2.- Binding energy curves of the three high-symmetry stacking modes of the strained mode system *I*, the lines are just guides for the eyes. The inset displays the corresponding structures. AB_I and AA_I are the optimal and worst stacking modes of *h*-BNC$_2$/graphene model system.
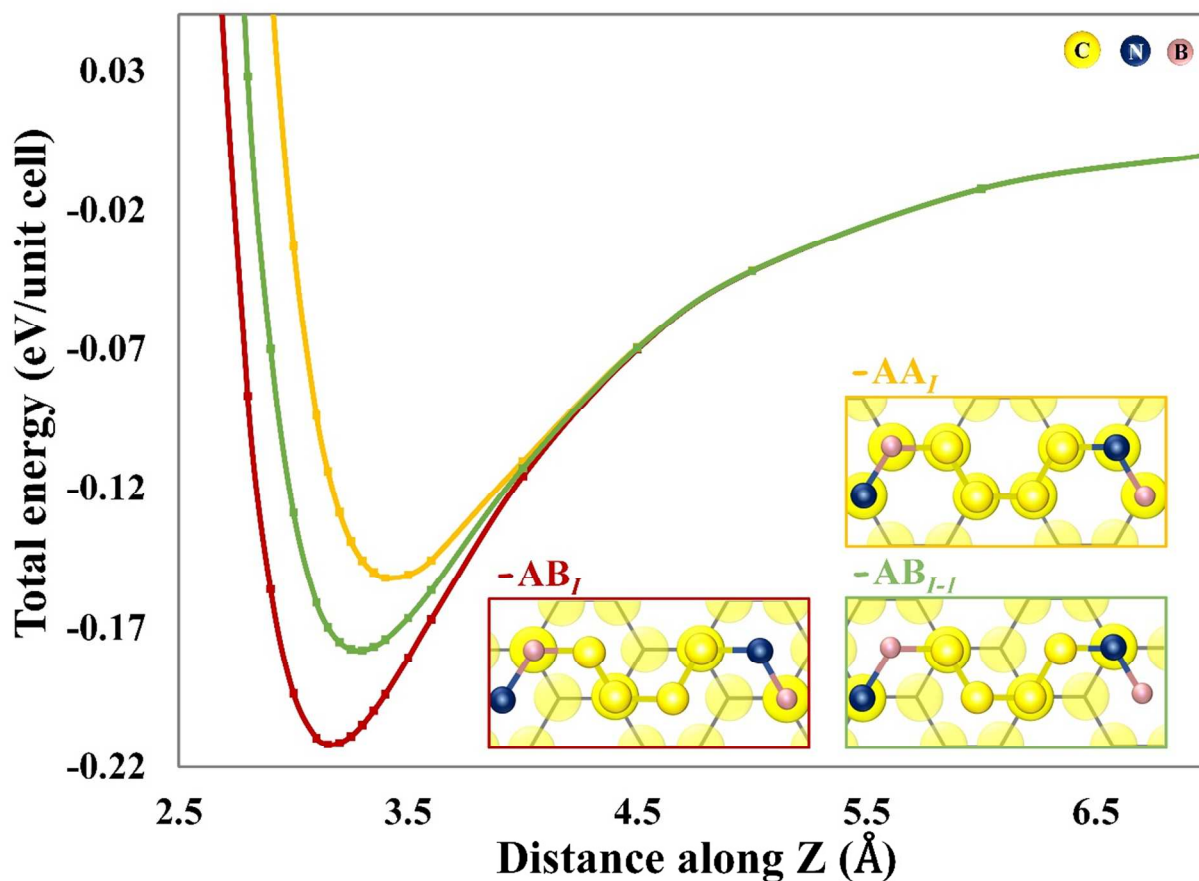
Figure 3.- Binding energy curves of the six high-symmetry stacking modes of the strained mode system *II*, the lines are just guides for the eyes. The inset displays the structure of the corresponding structures. AB_{II} and AA_{II} are the optimal and worst stacking modes of *h*-BNC_2/*h*-BN model system.
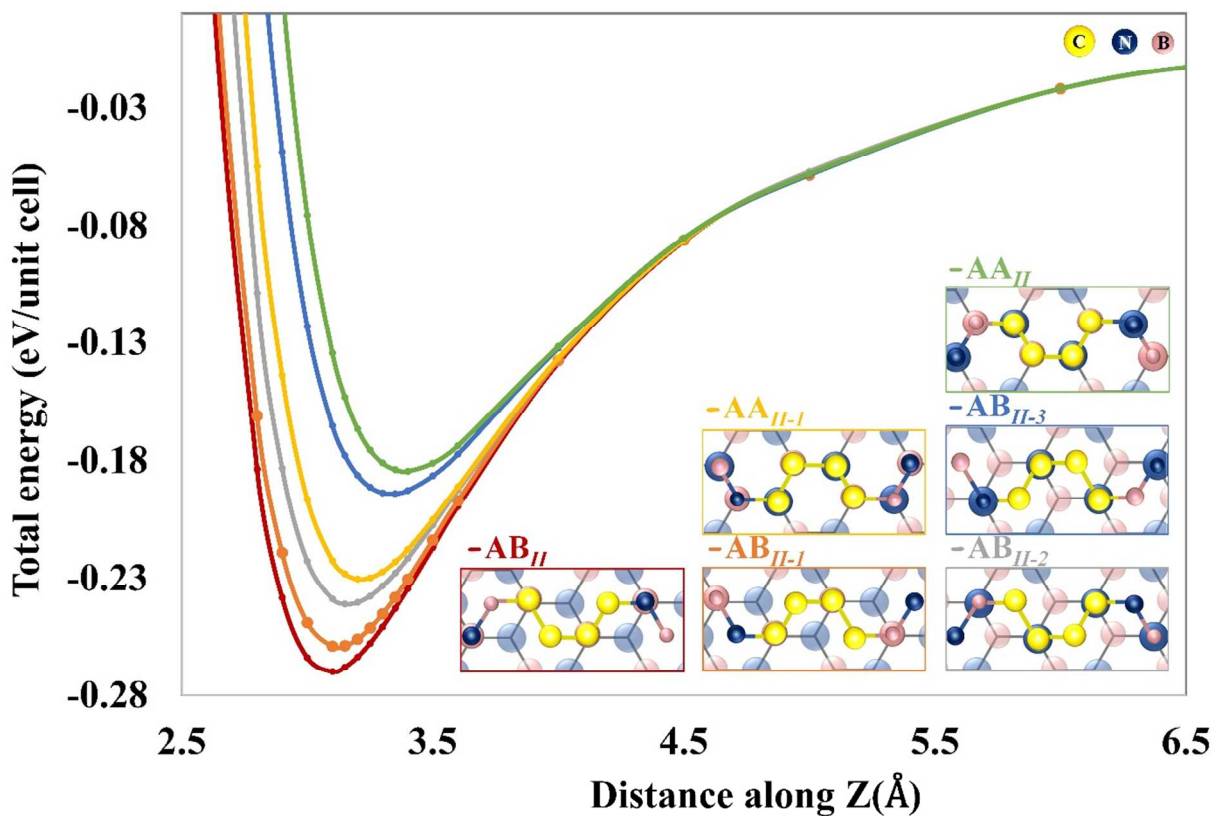
Figure 4.- Binding energy curves of the fourteen high-symmetry stacking modes of the strained mode system *III*, the lines are just guides for the eyes. The inset provides the structure of the corresponding structures. AB_{III} and AA_{III} are the optimal and worst stacking modes of *h*-BNC_2/graphene model system.
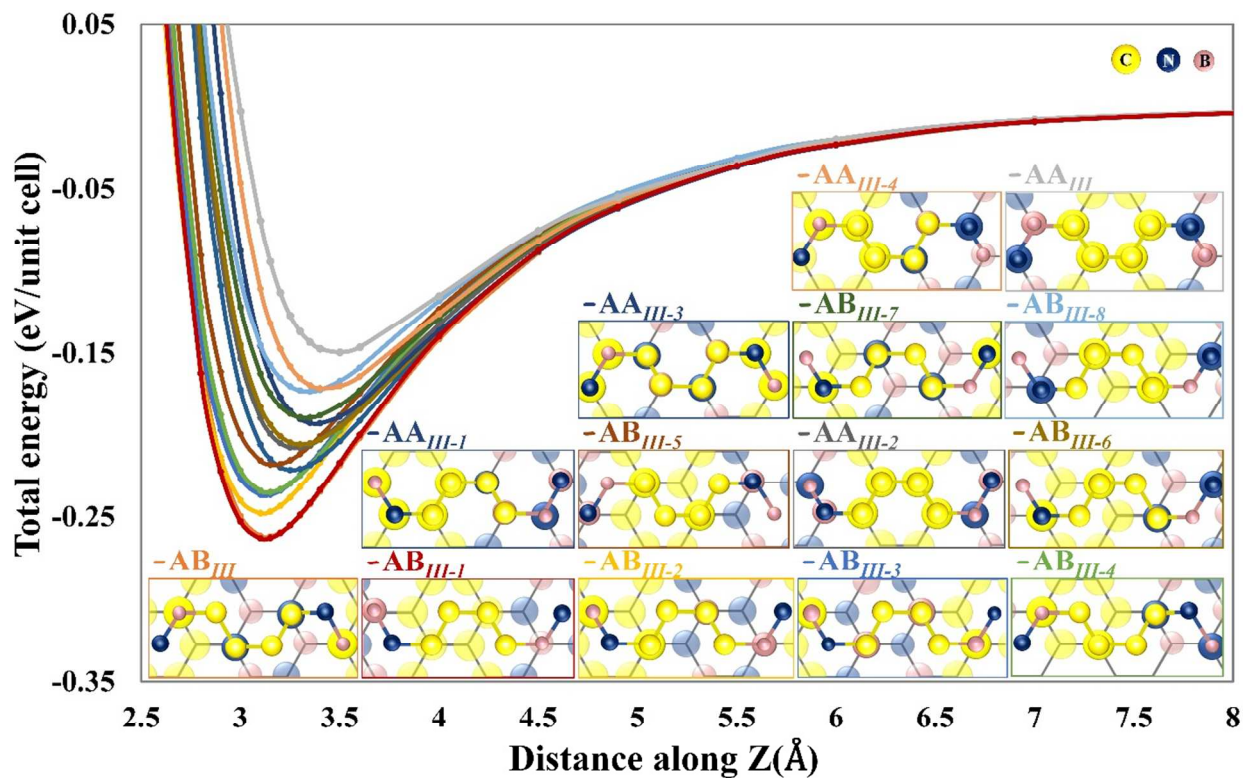
Figure 5.- Binding energy of different high symmetry stacking modes for *I* (green), *II* (yellow) and *III* (orange) model systems with respect to the optimal staking modes, respectively. Lines are just guides for the eyes. The inset reports plots of $\Delta e_{eq} = e_{AA} - e_{AB}$ and $\Delta Z_{eq} = Z_{AA} - Z_{AB}$.
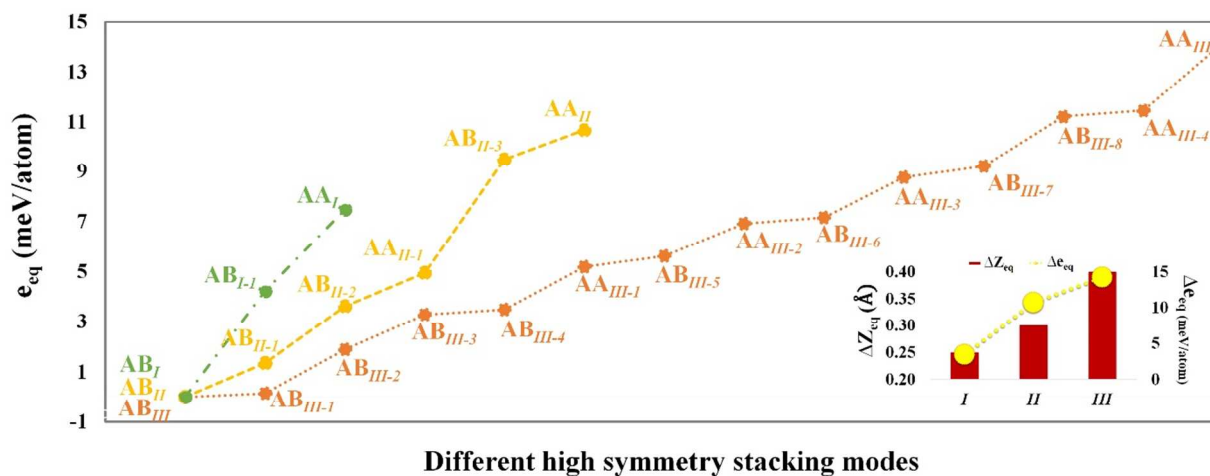
Figure 6.- Band structure of the graphene (a); h-BN (b); h-BNC$_2$ (c) monolayers and h-BNC$_2$/graphene (d); h-BNC$_2$/h-BN (e); h-BNC2/h-BNC$_2$ (f) bilayers. The band structure of the optimal and worst stacking modes are superimposed to better evidence the effect of stacking.
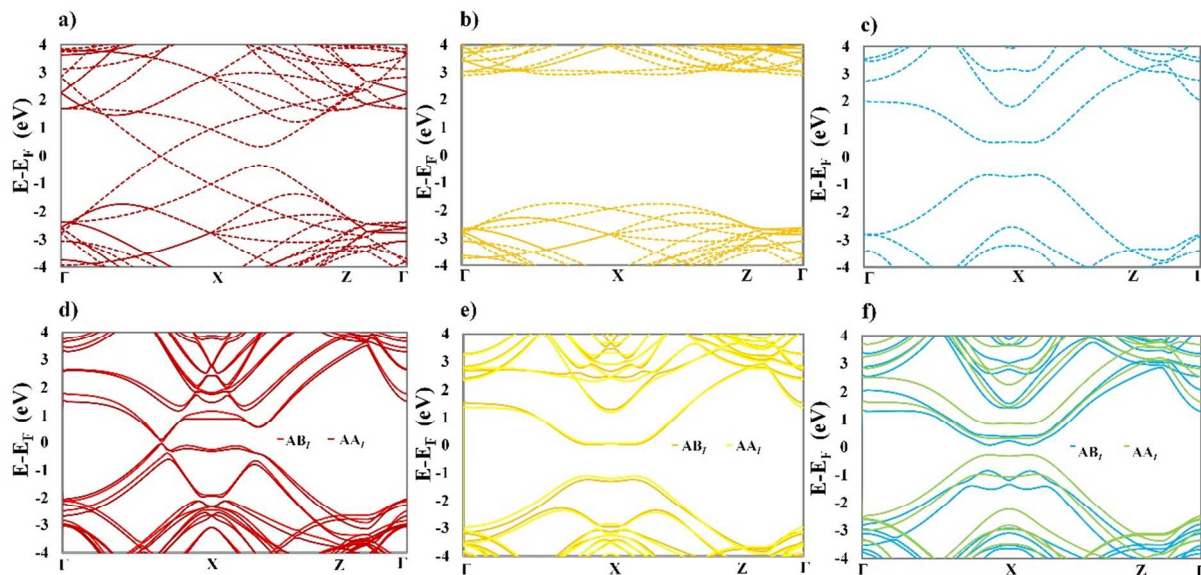
Figure 7.- ISEL as predicted by the DFT-D based method for (a) *I*, (b) *II* and (c) *III* bilayers and ISEL by the best fits registry index for (d) *I*, (e) *II* and (f) *III* bilayer model systems.
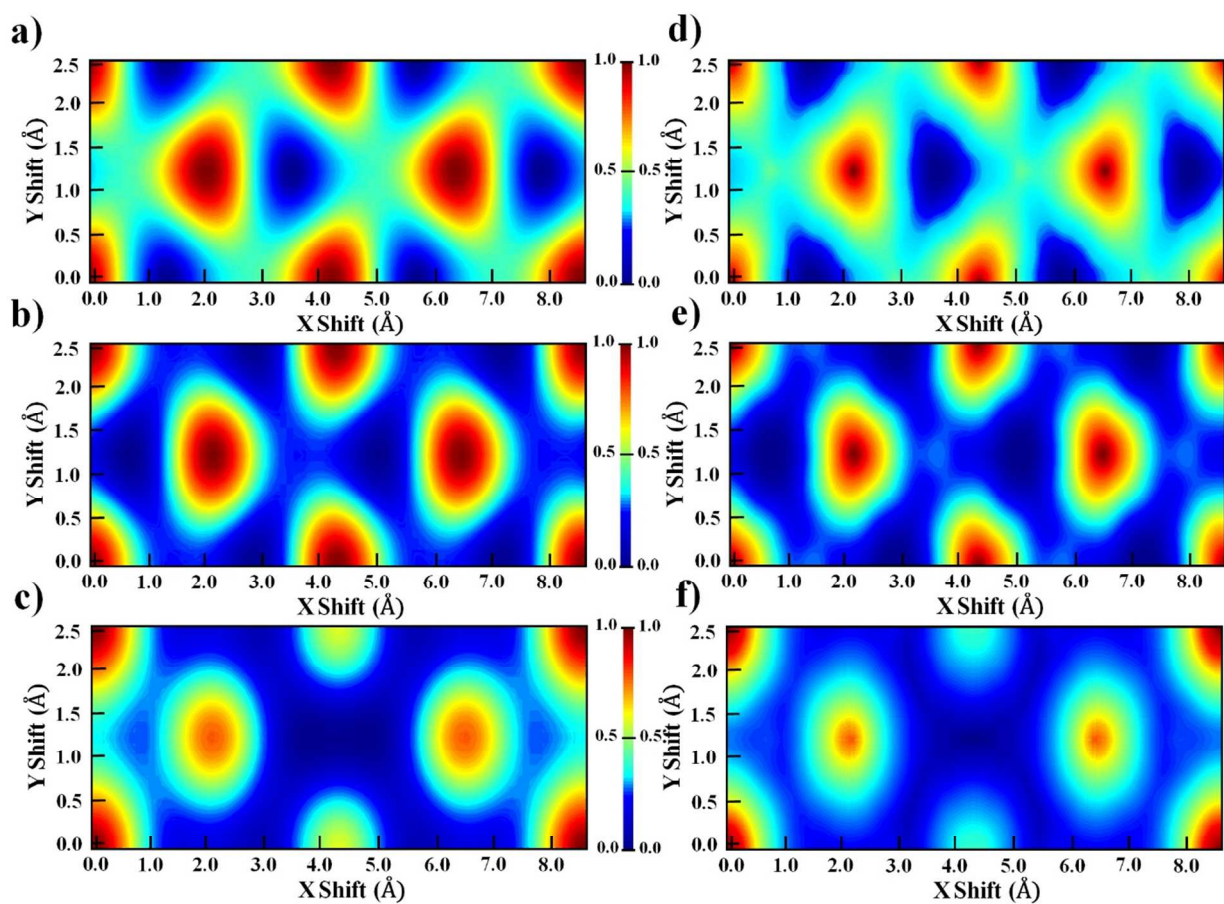
Figure 8.- Effect of flake size and misfit angle on the corrugation of the sliding RI surface of the heterogeneous h-BNC$_2$/graphene interface. (a) Schematic representation of a square 72×42 h-BNC$_2$ flake on top of an graphene layer with a misfit angle of 0°; (b) Maximal variations of the RI calculated along linear paths in the sliding direction as a function of interlayer misfit angle. The inset shows maximal RI corrugation as a function of flake size (number of atoms in the flake). The different diagrams presented in panel (b) are normalized as to the size of the relevant h-BNC$_2$ flake such that a maximal RI corrugation of 1 is obtained for a strained h-BNC$_2$ flake consisting of the same number of atoms and geometry having no lattice mismatch with the underlying graphene layer.

a)

b)
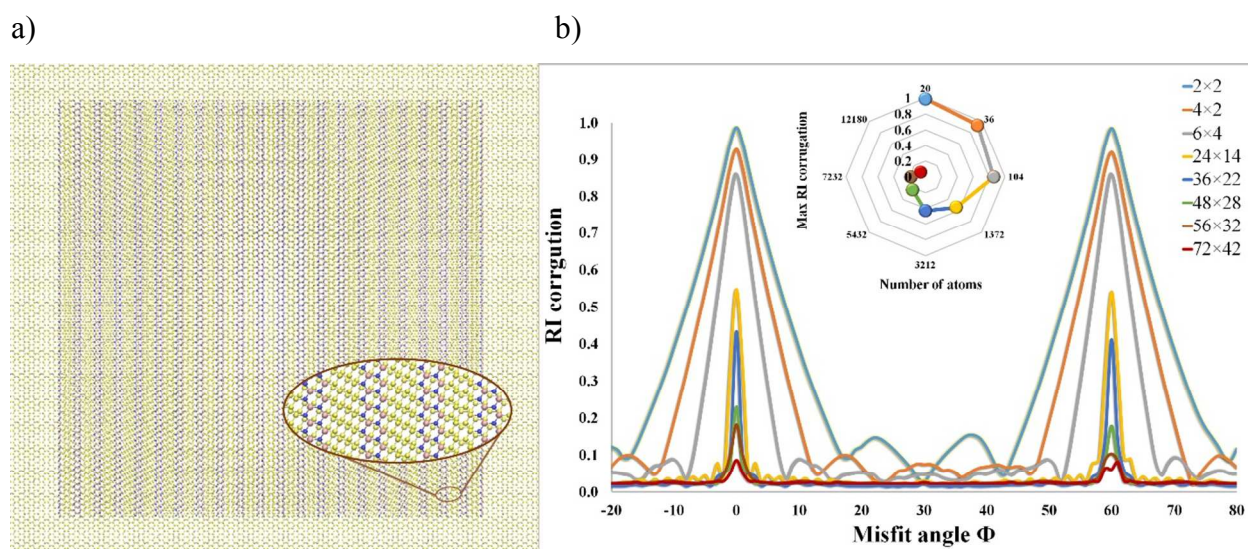
Figure 9.- Effect of flake size and misfit angle on the corrugation of the sliding RI surface of the heterogeneous h-BNC$_2$/h-BN interface. (a) Schematic representation of a square 72×42 h-BNC$_2$ flake on top of an graphene layer with a misfit angle of 45°. (b) Maximal variations of the RI calculated along linear paths in the sliding direction as a function of interlayer misfit angle. (Inset) Maximal RI corrugation as a function of flake size (number of atoms in the flake). The different diagrams presented in panel (b) are normalized as in Figure 9.
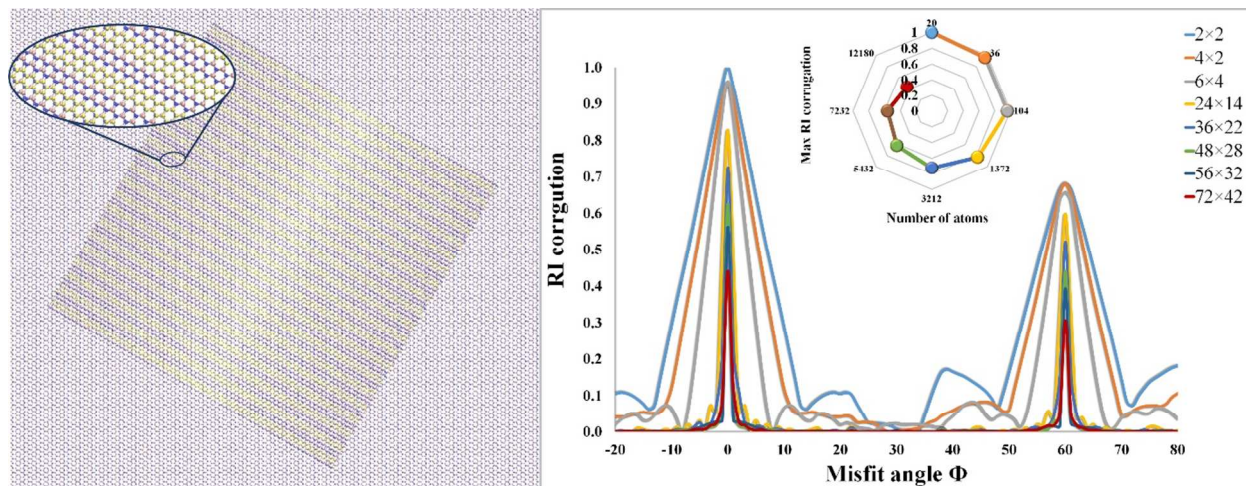
Figure 10.- Effect of flake size and misfit angle on the corrugation of the sliding RI surface of the heterogeneous h-BNC$_2$/ h-BNC$_2$interface. (a) Schematic representation of a square 72×42 h-BNC$_2$ flake on top of an graphene layer with a misfit angle of -20°. (b) Maximal variations of the RI calculated along linear paths in the sliding direction as a function of interlayer misfit angle. (Inset) Maximal RI corrugation as a function of flake size (number of atoms in the flake). The different diagrams presented in panel (b) are as in Figure 9.
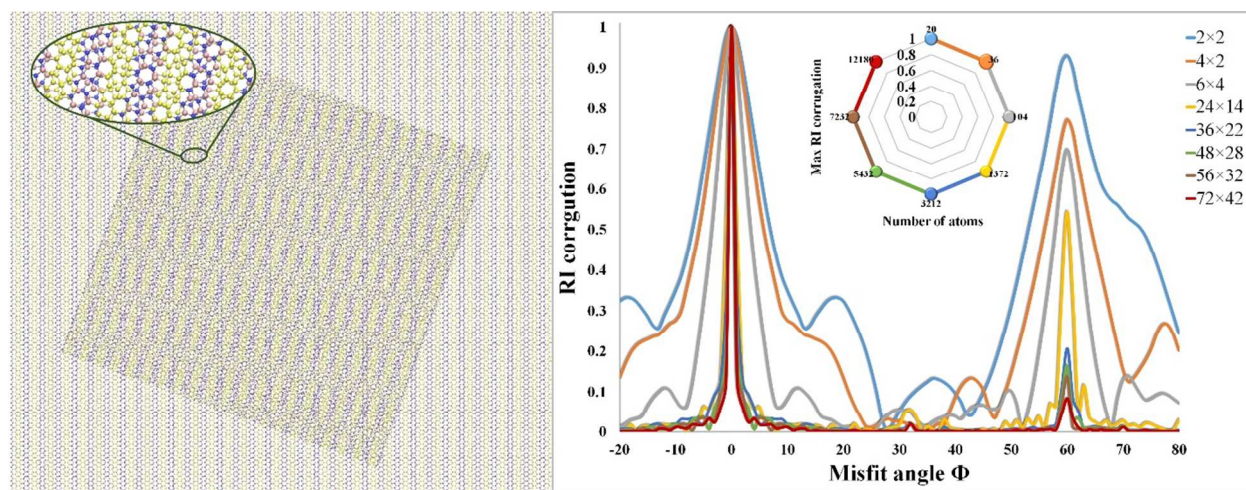
References

[1] D. Bonnell, Scanning Probe Microscopy and Spectroscopy: Theory, Techniques, and Applications; Ed.; Wiley VCH: New York, 2000.

[2] B. N. J. Persson, J. Chem. Phys., 2001, 115, 3840-3861.

[3] B. Bhushan, J. N. Israelachvili and U. Landman, Nature, 1995, 374, 607-616.

[4] R. W. Carpick and M. Salmeron, Chem. Rev., 1997, 97, 1163-1194.

[5] Z. Deng, A. Smolyanitsky, Q. Y. Li, X. Q. Feng and R. J. Cannara, Nature Mater., 2012, 11, 1032-1037.

[6] M. Enachescu, R. J. A. van den Oetelaar, R. W. Carpick, D. F. Ogletree, C. F. J. Flipse and M. Salmeron, Phys. Rev. Lett., 1998, 81, 1877-1880.

[7] S. Fujisawa, E. Kishi, Y. Sugawara and S. Morita, Phys. Rev. B, 1995, 52, 5302-5305.

[8] E. Gnecco, R. Bennewitz, T. Gyalog and E, Meyer, J. Phys.: Condens. Matter, 2001, 13, R619-R642.

[9] C. M. Mate, G. M. Mcclelland, R. Erlandsson and S. Chiang, Phys. Rev. Lett., 1987, 59, 1942-1945.

[10] U. D. Schwarz, O. Zworner, P. Koster and R. Wiesendanger, Phys. Rev. B, 1997, 56, 6987-6996.

[11] A. Vanossi, N. Manini, M. Urbach, S. Zapperi and E. Tosatti, Rev. Mod. Phys., 2013, 85, 529-552.

[12] J. Y. Park and M. Salmeron, Chem. Rev., 2014, 114, 677-711.

[13] T. Cohen-Karni, L. Segev, O. Srur-Lavi, S. R. Cohen and E. Joselevich, Nat. Nanotechnol., 2006, 1, 36-41.

[14] M. S. Bresnehan, M. J. Hollander, M. Wetherington, M. LaBella, K. A. Trumbull, R. Cavalero, D. W. Snyder, J. A. Robinson, ACS Nano, 2012, 6, 5234-5241

[15] R. T. Paine and C. K. Narula, Chem. Rev., 2014, 90, 73-91.

[16] Y. Lin and J. W. Connell, Nanoscale, 2012, 4, 6908- 6939.

[17] Q. Tang and Z. Zhou, Prog. Mater. Sci., 2013, 58, 1244- 1315.

[18] A. C. Neto, F. Guinea, N. Peres, K. S. Novoselov and A. K. Geim, Rev. Mod. Phys., 2009, 81, 109-162.

[19] A. Nagashima, Y. Gamou, M. Terai, M. Wakabayashi and C. Oshima, Phys. Rev. B, 1996, 54, 13491-13494.

[20] L. D. Carr and M. T. Lusk, Nature Nanotechnol., 2010, 5, 316-317.

[21] K. Yuge, Phys. Rev. B, , 79, 144109-6.

[22] J. M. Pruneda, Phys. Rev. B, 2010, 81, 161409(R)-4.

[23] J. Zhu, S. Bhandary, B. Sanyal and H. Ottosson, J. Phys. Chem. C, 2014, 115, 10264- 10271.

[24] J. da Rocha Martins and H. Chacham, ACS Nano, 2014, 5, 385-393.

[25] A. Y. Liu, R. M. Wentzcovitch and M. L. Cohen, Phys. Rev. B, 1989, 39, 1760-1765.

[26] C.-K. Chang, S. Kataria, C.-C. Kuo, A. Ganguly, B.-Y. Wang, J.-Y. Hwang, K.-J. Huang, W.-H. Yang, S.-B. Wang, C.-H. Chuang, M. Chen, C.-I. Huang, W.-F. Pong, K.-J. Song, S.-J. Chang, J.-H. Guo, Y. Tai, M. Tsujimoto, S. Isoda, C.-W. Chen, L.-C. Chen and K.-H. Chen, ACS Nano, 2014, 7, 1333- 1341.

[27] G. Bepete, D. A. Voiry, M. Chhowalla, Z. Chiguvare and N. J. Coville, Nanoscale, 2013,5, 6552- 6557.

[28] P. Srivastava, M. Deshpande and P. Sen, Phys. Chem. Chem. Phys., 2011, 13, 21593-21599.

[29] L. Ci, L. Song, C. Jin, D. Jariwala, D. Wu, Y. Li, A. Srivastava, Z. Wang, K. Storr and L. Balicas, Nat. Mater., 2010, 9, 430-435.

[30] N. Kumar, K. Moses, K. Pramoda, S. N. Shirodkar, A. K. Mishra, U. V. Waghmare, A. Sundaresan and C. N. R. Rao, J. Mater. Chem. A, 2013,1, 5806-5821.

[31] M. O. Watanabe, S. Itoh, T. Sasaki and K. Mizushima, Phys. Rev. Lett., 1996, 77, 187- 189.

[32] K. S. Nagapriya, O. Goldbart, I. Kaplan-Ashiri, G. Seifert, R. Tenne and E. o Joselevich, Phys. Rev. Lett., 2008, 101, 195501-4.

[33] O. Hod and G. E. Scuseria, Nano Lett., 2009, 9, 2619- 2622.

[34] T. Rueckes, K. Kim, E. Joselevich, G. Y. Tseng, C.-L. Cheung and C. M. Lieber, Science, 2000, 289, 94-97.

[35] T. W. Tombler, C. Zhou, L. Alexseyev, J. Kong , H. Dai , L. Liu, C. S. Jayanthi, M. Tang and S.-Y. Wu, Nature, 2000, 405, 769-772.

[36] C. Stampfer, A. Jungen, R. Linderman, D. Obergfell, S. Roth and C. Hierold, Nano Lett., 2006, 6, 1449-1453.

[37] I. Leven, D. Krepel, O. Shemesh and O. Hod, J. Phys. Chem. Lett., 2013, 4, 115-120.

[38] L. Song, L. Ci, C. Jin, D. Jariwala, D. Wu, Y. Li, A. Srivastava, Z. F. Wang, K. Storr, L. Balicas, F. Liu and P. M. Ajayan, Nat. Mater., 2010, 9, 430-435.

[39] J. Zhu, S. Bhandary, B. Sanyal and H. Ottosson, J. Phys. Chem. C, 2011, 115, 10264- 10271.

[40] X. Wu, M. C. Vargas, S. Nayak, V. Lotrich, and G. J. Scoles, Chem. Phys., 2001, 115, 8748- 8757.

[41] P. Giannozzi, S. Baroni, N. Bonini, M. Calandra, R. Cavazzoni, C. Car, D. Ceresoli, G. L. Chiarotti, M. Cococcioni and I. Dabo, J. Phys.: Condens. Matter, 2009, 21, 395502- 395521.

[42] J. P. Perdew, K. Burke and M. Ernzerhof, Phys. Rev. Lett., 1996, 77, 3865- 3868.

[43] J. P. Perdew and M. Levy, Phys. Rev. Lett., 1983, 51, 1884–1887.

[44] L. J. Sham and M. Schluter, Phys. Rev. Lett., 1983, 51, 1888–1891.

[45] W. E. Pickett, Comput. Phys. Rep., 1989, 9, 115-197.

[46] D. Vanderbilt, Phys. Rev. B, 1990, 41 , 7892-7895.

[47] N. Marom, J. Bernstein, J. Garel, A. Tkatchenko, E. Joselevich, L. Kronik and O. Hod, Phys. Rew. Lett., 2010, 105, 046801-4.

[48] O. Hod, Isr. J. Chem., 2010, 50, 506-514.

[49] O. Hod, Chem. Phys. Chem., 2013, 14, 2376- 2391.

[50] N. Marom, J. Bernstein, J. Garel, A. Tkatchenko, E. Joselevich, L. Kronik and O. Hod, Phys. Rev. Lett., 2010, 105, 046801-4.

[51] A. Bosak, M. Krisch, M. Mohr, J. Maultzsch and C. Thomsen, Phys. Rev. B, 2007, 75, 153408-4.

[52] C. Lee, X. Wei, J. W. Kysar and J. Hone, Science, 2008, 321, 385−388.

[53] A. Bosak, J. Serrano, M. Krisch, K. Watanabe, T. Taniguchi and H. Kanda, Phys. Rev. B 2006, 73, 041402-4.

[54] P. H. Tan, W. P. Han, W. J. Zhao, Z. H. Wu, K. Chang, H. Wang, Y. F. Wang, N. Bonini, N. Marzari, N. Pugno, G. Savini, A. Lombardo and A. C. Ferrari, Nat. Mater., 2012, 11, 294−300.

[55] M. Grimsditch, J. Phys. C: Solid State Phys. 1983, 16, L143.

[56] Q. Peng, A. R. Zamiri, W. Ji and S. De, Acta. Mech., 223, 2012, 2591–2596

[57] O. Hod, Phys. Rev. B, 2012, 86, 075444-8.